

**Vapor phase processing of  $\alpha$ -Fe<sub>2</sub>O<sub>3</sub> photoelectrodes  
for water splitting:  
an insight into the structure/property interplay**

Michael E. A Warwick<sup>1</sup>, Kimmo Kaunisto<sup>1,2</sup>, Davide Barreca<sup>3,\*</sup>, Giorgio Carraro<sup>1</sup>, Alberto Gasparotto<sup>1</sup>, Chiara Maccato<sup>1</sup>, Elza Bontempi<sup>4</sup>, Cinzia Sada<sup>5</sup>, Tero-Petri Ruoko<sup>2</sup>, Stuart Turner<sup>6</sup>, Gustaaf Van Tendeloo<sup>6</sup>

<sup>1</sup>*Department of Chemistry, Padova University and INSTM, 35131 Padova, Italy.*

<sup>2</sup>*Department of Chemistry and Bioengineering, Tampere University of Technology, 33101 Tampere, Finland.*

<sup>3</sup>*CNR-IENI and INSTM, Department of Chemistry, Padova University, 35131 Padova, Italy.*

<sup>4</sup>*Chemistry for Technologies Laboratory, University of Brescia, 25123 Brescia, Italy.*

<sup>5</sup>*Department of Physics and Astronomy, Padova University, 35131 Padova, Italy.*

<sup>6</sup>*EMAT, University of Antwerp, 2020 Antwerpen, Belgium.*

\*Corresponding author. E-mail address: [davide.barreca@unipd.it](mailto:davide.barreca@unipd.it) (D. Barreca).

## Abstract

Harvesting radiant energy to trigger water photoelectrolysis and produce clean hydrogen is receiving increasing attention in the search of alternative energy resources. In this regard, *hematite*( $\alpha$ -Fe<sub>2</sub>O<sub>3</sub>) nanostructures with controlled nano-organization have been fabricated and investigated for use as anodes in photoelectrochemical (PEC) cells. The target systems have been grown on conductive substrates by a plasma enhanced-chemical vapor deposition (PE-CVD) approach and subjected to eventual *ex-situ* annealing in air at temperatures > 600°C in order to further tailor their structure and properties. A detailed multi-technique approach has enabled to elucidate the interrelations between system characteristics and the generated photocurrent.

The present  $\alpha$ -Fe<sub>2</sub>O<sub>3</sub> systems are characterized by a high purity and hierarchical morphologies consisting of nanopylramids/organized dendrites, offering a high contact area with the electrolyte. PEC data reveal a dramatic response enhancement upon thermal treatment, related to a more efficient electron transfer. The reasons underlying such a phenomenon are also elucidated and discussed by analyzing the kinetics of photogenerated charge carriers.

## Keywords

hematite, PE-CVD, hierarchical structures, water splitting, PEC, transient absorption spectroscopy

## Introduction

The conversion of solar energy into hydrogen by means of photoelectrochemical water splitting is emerging as a sustainable area to meet global energy demands in a carbon-neutral fashion [1-10]. This strategy offers an amenable option to yield pure hydrogen, a clean and storable energy carrier that, in turn, can be converted into electrical power, becoming a key tool of the future world energy economy [11-17]. So far, numerous inorganic semiconductors (e.g.  $\text{WO}_3$ ,  $\text{TiO}_2$ ,  $\text{BiVO}_4$ ,...) have been fabricated towards the goal of producing a high-efficiency PEC system for  $\text{H}_2$  generation [3-7, 10, 14-16, 18-20]. Compared with other metal oxides,  $\alpha\text{-Fe}_2\text{O}_3$  (*hematite*), the most stable form of iron(III) oxide at room temperature, is one of the most promising candidates for the development of Vis-light absorbing photoanodes [13, 21-26]. Beyond the favourable band-gap ( $E_G = 2.1$  eV) [19, 22, 27-33], its main advantages are in fact its abundance, low cost, non-toxicity and high chemical stability [32, 34], also in alkaline environment [1, 4, 12, 19, 35]. Nevertheless, these benefits are eclipsed by the slow reaction kinetics [5, 17, 36], poor charge transport properties [7, 16] and short hole diffusion length [9, 20, 29, 30, 33], along with comparatively long light penetration depths [2, 11, 18, 28]. Overall, these phenomena result in an ultra-fast electron-hole recombination in a ps timescale, followed by electron trapping in a ps to  $\mu\text{s}$  timescale and bulk recombination in a  $\mu\text{s}$  to ms timescale [2, 37-40]. On the other hand, water oxidation has been shown to occur in a subsecond-second scale [14, 41], making imperative the need of longer charge carrier lifetimes to effectively drive the overall process [6, 29].

To circumvent these drawbacks and promote increased functional performances, various synthesis and modification strategies have been adopted [17, 34, 42]. The main ones involve doping/functionalization of  $\alpha\text{-Fe}_2\text{O}_3$  with suitable systems [1, 5, 19, 23, 30, 36], in order to increase Vis light absorption and/or promote oxygen evolution [2, 4, 6, 26, 29], or appropriate nanoarchitecture designing [20, 28, 35, 43, 44], to decrease recombination losses

[21, 33, 45]. In particular, nanostructured photoelectrode architectures have begun to address *hematite* limitations by decoupling light absorption and charge carrier extraction [1, 7, 15, 30]. Representative examples span from nanotubes, to nanoplatelets and dendritic structures [2, 11, 13, 17, 20, 24, 29], resulting in a higher contact area with the electrolyte [6-8, 29] and increasing the number of holes available for H<sub>2</sub>O oxidation, minimizing recombination losses [1, 2, 5, 11, 22, 44].

While great strides have been taken to improve the performance and understanding of H<sub>2</sub>O oxidation with *hematite* electrodes, the state-of-the-art is still far from optimal and there are several fundamental issues which need to be better understood [4, 16]. In fact, many studies have been devoted to the use of wet chemical/colloidal routes, hardly enabling a simultaneous control of morphology and doping level and resulting in poor carrier collection and transport [20, 28, 42]. To overcome these disadvantages and obtain improved PEC performances, *ex-situ* thermal treatments have been used by various investigators [4, 5, 7, 10-13, 15, 17, 19, 20, 22, 35]. Never the less, a detailed study of photogenerated charge carrier dynamics as a function of system thermal processing is still missing and deserves further studies [15].

With this background in mind, we report here on *hematite* ( $\alpha$ -Fe<sub>2</sub>O<sub>3</sub>) nanostructures with a hierarchical morphology. The target systems have been obtained by PE-CVD on fluorine-doped tin oxide (FTO) substrates at 300-400°C and subsequently subjected to suitable thermal treatments in air to tailor the system structure, composition and optical absorption. So far, only a few studies have been devoted to the PE-CVD of *hematite* for PEC applications [8, 9, 11], in spite of the great potential and industrial scalability of this technique [46].

The interrelations between the material chemico-physical properties and the processing conditions are investigated in detail by a number of complementary techniques. For the first time, the PEC performances of PE-CVD Fe<sub>2</sub>O<sub>3</sub> nanomaterials as a function of annealing treatments is elucidated by the use of transient absorption spectroscopy (TAS), that enables a

direct monitoring of photogenerated charge carrier dynamics during PEC water oxidation [2, 14, 25, 47, 48].

## 1. Experimental

### 1.1. Synthesis

Fe<sub>2</sub>O<sub>3</sub> nanomaterials were grown *via* PE-CVD on conductive FTO-coated glass slides (Aldrich, 735167-1EA,  $\approx 7 \Omega/\text{sq}$ ; lateral dimensions = 2.0 cm  $\times$  1.0 cm; FTO thickness  $\approx$  600 nm), cleaned prior to each deposition by a previously reported procedure [44, 46]. Growth experiments were performed at substrate temperatures of 300 and 400°C for a total duration of 1 h (total pressure = 1.0 mbar; RF-power = 10 W). The obtained samples were characterized both as-grown and after *ex-situ* thermal treatments in air at 650°C for 1 h, selected as an optimal temperature basing on previous studies [20]. In the following, specimens will be labelled according to Table 1 as a function of their growth temperature and annealing conditions. Further details on the instrumental apparatus and the adopted synthesis conditions are reported in the Electronic Supplementary Material (ESM).

### 1.2. Characterization

X-ray diffraction (XRD) measurements were carried out operating in reflection mode by means of a Dymax-RAPID microdiffractometer equipped with a cylindrical imaging plate detector, allowing data collection from 0 to 160° (2 $\theta$ ) horizontally and from -45 to +45° (2 $\theta$ ) vertically upon using CuK $\alpha$  radiation ( $\lambda = 1.54056 \text{ \AA}$ ). Each pattern was collected with an exposure time of 40 min, using a collimator diameter of 300  $\mu\text{m}$ . Conventional XRD patterns were then obtained by integration of 2D images.

X-ray photoelectron spectroscopy (XPS) analyses were conducted on a Perkin-Elmer  $\Phi$  5600ci apparatus with a standard AlK $\alpha$  radiation ( $h\nu = 1486.6 \text{ eV}$ ), at pressures  $< 10^{-8}$  mbar.

Charge correction was performed by assigning to the adventitious C1s signal a Binding Energy (BE) of 284.8 eV[49]. After a Shirley-type background subtraction, atomic percentages (at.%) were calculated by signal integration using standard PHI V5.4A sensitivity factors. Ar<sup>+</sup> sputtering was carried out at 4.0 kV, with an argon partial pressure of  $\approx 5 \times 10^{-8}$  mbar.

Secondary ion mass spectrometry (SIMS) investigation was carried out by means of a IMS 4f mass spectrometer (Cameca) using a Cs<sup>+</sup> primary beam (voltage = 14.5 keV; current = 25 nA, stability = 0.2%) and negative secondary ion detection, adopting an electron gun for charge compensation. Beam blanking mode and high mass resolution configuration were adopted. Signals were recorded rastering over a  $150 \times 150 \mu\text{m}^2$  area and detecting secondary ions from a sub region close to  $10 \times 10 \mu\text{m}^2$  to avoid crater effects.

Atomic force microscopy (AFM) analyses were carried out using a NT-MDT SPM Solver P47H-PRO instrument operating in semicontact/tapping mode and in air. After plane fitting, Root-Mean-Square (RMS) roughness values were obtained from  $3 \times 3 \mu\text{m}^2$  images.

The system nano-organization was further characterized through a Zeiss SUPRA 40 VP field emission-scanning electron microscopy (FE-SEM) instrument, operating at primary beam acceleration voltages comprised between 5.0 and 10.0 kV. Thickness values (Table 1) were obtained from the statistical analysis of cross-sectional micrographs.

Optical absorption spectra were recorded in transmission mode at normal incidence by a Cary 50 spectrophotometer, using bare FTO glass as a reference. In all cases, the substrate contribution was subtracted.

PEC measurements (see also ESM for further details) were carried out in a three-electrode cell, with *hematite* nanodeposits as working electrodes. An Ag/AgCl/KCl (3 M) and a Pt mesh were used as reference and counter-electrodes, respectively. An aqueous NaOH solution (pH = 13.6), previously purged with N<sub>2</sub> for 30 min, was used as electrolyte. A

PARSTAT 2273 potentiostat was used for current-voltage measurements under simulated solar light (AM 1.5G; irradiation intensity = 100 mW/cm<sup>2</sup>).

Transmission electron microscopy (TEM) and electron diffraction (ED) experiments were carried out on a FEI Tecnai Osiris microscope, operated at 200 kV and equipped with a Super-X high solid angle energy-dispersive X-ray (EDX) detector. High resolution high-angle annular dark field scanning transmission electron microscopy (HAADF-STEM) and high resolution TEM (HRTEM) images were acquired on a FEI Titan “cubed” microscope (acceleration voltage = 300 kV), equipped with an aberration corrector for the probe-forming and image-forming lens.

TAS analyses were performed on specimens having a geometric area of 3×3 cm<sup>2</sup> in a complete PEC cell (Zahner-elektrik PECC-2). To simulate the conditions of the above PEC experiments, a three-electrode configuration was used with a Pt counter-electrode, an Ag/AgCl (3M KCl) reference electrode and a NaOH electrolyte, degassed with N<sub>2</sub> prior to experiments. Measurements were carried out by a modified flash-photolysis apparatus (Luzchem LFP-111) with a New Focus (model 2051) photodetector and a halogen lamp (9 W, Thorlabs SLS201/M) probe (see also ESM for further details).

## 2. Results and Discussion

Initial efforts were devoted to the fabrication of α-Fe<sub>2</sub>O<sub>3</sub> systems endowed with the following characteristics [13]: a) improved crystallinity, with reduced content of charge trapping defects; b) porous non-isotropic morphology, enabling a higher active area.

The as-prepared materials appear semi-transparent and orange-red, and upon annealing at 650°C a slight colour darkening is observed (Figure 1) [5, 28]. Figure 1 displays XRD patterns of as-prepared and annealed systems. Apart from prominent peaks related to FTO, that dominate the recorded patterns, the diffraction signals located at  $2\theta = 24.1, 33.1, 35.6, 40.8$

1 and 49.4° can be attributed to (012), (104), (110), (113) and (024) reflections of the  
2 rhombohedral *hematite* phase [50]. No other signals could be observed, indicating the  
3 absence of other Fe<sub>2</sub>O<sub>3</sub> polymorphs. Irrespective of the adopted growth temperature, thermal  
4 processing results in a progressive enhancement the (110) reflection. This phenomenon, in  
5 accordance with previous observations [10, 42], may suggest a preferential alignment of the  
6 [110] axis perpendicularly to the substrate (being a *c*-oriented growth). In particular, the  
7 (110)/(012) intensity ratios, systematically higher than in the case of α-Fe<sub>2</sub>O<sub>3</sub> powder  
8 diffractogram [50], underwent an increase with the processing temperature according to the  
9 order 300<400<300\_A<400\_A (see Table 1).  
10  
11  
12  
13  
14  
15  
16  
17  
18  
19  
20

21 It has been reported that *hematite* has a much higher conductivity along the [110] direction  
22 with respect to the orthogonal ones, such as [001] (Figure 1c) [24, 35, 43]. As a consequence,  
23 the above mentioned preferred orientation may account for an improved electron transport  
24 through annealed specimens, facilitating the collection of photogenerated electrons [4, 5] and  
25 resulting in enhanced PEC performances (see below and Figure6) [10, 19].  
26  
27  
28  
29  
30  
31  
32  
33

34 In order to analyze the chemical composition, XPS and SIMS analyses were carried out.  
35 Figure 2a compares representative XPS wide-scan spectra for the target nanosystems before  
36 and after the annealing treatment. The analysis of the O/Fe ratio shows no statistically  
37 relevant evidence that oxygen deficiencies are playing a major role in the electrode  
38 photoactivity [28], at variance with previous studies [10]. The average O/Fe values close to  
39 1.7, slightly higher than the stoichiometric one expected for Fe<sub>2</sub>O<sub>3</sub>, were related to surface  
40 hydroxylation [see also Figure S-1 in the ESM]. Irrespective of the experimental conditions,  
41 the Fe2p peak shape and position [BE(Fe2p<sub>3/2</sub>) = 711.2 eV], along with the spin orbit  
42 separation of 13.4eV [4, 30, 36, 44, 51], are in agreement with the presence of Fe(III) in an  
43 oxide environment, free from other iron oxidation states [8, 17, 19, 31, 46, 49, 52].  
44  
45  
46  
47  
48  
49  
50  
51  
52  
53  
54  
55  
56  
57

58 Preliminary studies on the in-depth system composition were carried out by XPS depth  
59  
60  
61  
62  
63  
64  
65



1 profiling on annealed systems. As regards the O1s peak (Figure 2b), the high BE tailing  
2 disappears after erosion, confirming that it arises from atmospheric exposure. The depth  
3 profile of the Fe2p region (Figure 2c) shows no significant variation, in line with the presence  
4 of pure iron(III) oxide in the target material. The good sample purity was confirmed also by  
5 the strong decrease of the C1s peak intensity upon sputtering [Figure S-2 in the ESM].  
6

7  
8  
9  
10  
11 More detailed information on the in-depth distribution of the various species was obtained by  
12 SIMS, and representative data are displayed in Figure 3. As a general rule, the specimen  
13 purity increases after thermal treatment, resulting in an average carbon content as low as  
14 tenths of ppm. Irrespective of the processing conditions, profiling in different specimen  
15 regions evidenced a parallel trend of Fe and O signals, suggesting their common chemical  
16 origin and confirming the homogeneous formation of iron(III) oxide, as also revealed by  
17 XPS. In addition, the data evidence a Sn tail extending into the nanodeposits, suggesting Sn  
18 diffusion from the FTO substrate into the material, at least to some extent. This phenomenon  
19 might result beneficial in view of PEC applications [30]. In fact, incorporation of tin into  
20 *hematite* has been reported to improve the system electrical conductivity [4, 5, 35] and to  
21 speed up the interfacial reaction of photogenerated holes [15].  
22

23  
24  
25  
26  
27  
28  
29  
30  
31  
32  
33  
34  
35  
36  
37  
38  
39  
40  
41  
42  
43  
44  
45  
46  
47  
48  
49  
50  
51  
52  
53  
54  
55  
56  
57  
58  
59  
60  
61  
62  
63  
64  
65  
Efforts were subsequently dedicated to the analysis of the deposit nano-morphology through  
the combined use of AFM and FE-SEM (Figure 4). For specimens grown at 300°C, AFM  
measurements reveal a fine arrangement of homogeneous nanoaggregates. AFM images  
enable to extract RMS roughness values, an important parameter in view of PEC applications  
[11] since an enhanced roughness is expected to correspond to a higher electrode/electrolyte  
interfacial area [34]. The values obtained in the present case are all very close to  $(20.0 \pm 1.5)$   
nm, and do not display any marked dependence on the processing conditions. In order to  
attain a deeper insight into the material morphology, FE-SEM analyses were undertaken,  
devoting particular attention not only to plane-view, but also to cross-sectional observations,

that are often not reported for FTO-supported photoelectrodes [5, 10, 18-20, 28, 34]. The results (Figure 4) evidence a system nano-organization based on two levels of hierarchical growth. In fact, sample **300** shows the presence of pyramidal aggregates as the smaller building blocks, possessing average dimensions of  $(80 \pm 20)$  nm. These particles are interconnected forming larger agglomerates with a mean length of  $(400 \pm 100)$  nm, and giving rise to a tightly packed cross-sectional arrangement. Similarly, specimen **400** displays the presence of dendritic structures [average sizes =  $(85 \pm 20)$  nm and  $(500 \pm 100)$  nm for the primary and secondary particles, respectively] evenly distributed over the FTO substrate. As shown by cross-sectional images, such dendrites appear vertically aligned with respect to the substrate, producing a relatively porous morphology. Such nanostructures may facilitate electron transport, allowing photogenerated holes to efficiently reach the interface with the electrolyte and improving the rate of charge transport relative to recombination [7, 42]. The presence of similar vertical arrays has also been reported to be beneficial for light trapping and scattering phenomena [20], which, in turn, enhance the nanomaterial light harvesting properties (see below).

In line with previous reports [10], the images of annealed samples show that the primary particles are bigger, more rounded and partially merged together, an effect more evident for specimen **300\_A**. In this case, the morphology is dominated by the presence of rounded elongated aggregates of  $(170 \pm 60)$  nm. For 400°C-deposited systems, a relatively similar particle structure is observed, although their morphology and shape is more reminiscent of the pristine nanodeposits, as evidenced by the bumped edges of larger agglomerates.

Despite RMS roughness values are very similar for all specimens (see above), cross-sectional FE-SEM micrographs registered after thermal treatment display the formation of more porous structures. The **300\_A** sample shows structures more rounded than in the pristine specimen, with the base areas almost fused into larger agglomerates. For the **400\_A** specimen, this

effect is slightly less pronounced, resulting in the formation of multi-particle agglomerates [primary particle average sizes =  $(90 \pm 30)$  nm; larger agglomerate dimensions =  $(450 \pm 100)$  nm]. Correspondingly, an increase in the mean nanodeposits thickness is observed (see Table 1). Overall, the annealing process seems to result in significant rearrangements leading to a decrease in grain boundary density, a phenomenon favourable for the system PEC performances (see below and Figure 6) [13], since it suppresses the recombination of photogenerated charge carriers [7, 19]. All together, these data demonstrate a higher degree of control on the system nano-organization hardly achievable by traditional chemical routes [4, 15, 19, 30, 36].

Since the optical absorption features of  $\alpha\text{-Fe}_2\text{O}_3$  are of great importance for solar energy conversion [28], the target nanosystems were also characterized by optical absorption spectroscopy (Figure 5). The absorption profiles are characterized by a sub-band-gap scattering tail in the 600-750 nm region [28], which increases in intensity upon annealing for both nanodeposits fabricated at 300 and 400°C. Concomitantly, data revealed the enhancement of a shoulder centred at  $\lambda \approx 540$  nm, typical of  $\alpha\text{-Fe}_2\text{O}_3$  films [7], related to spin-forbidden Fe(III) 3d→3d transitions [10, 13, 18, 42]. For all specimens, a sharp absorbance increase occurs from 550 - 600 nm towards lower wavelengths, consistently with the band-gap of *hematite* (see also below) [11, 13, 52]. In addition, in accordance with previous findings [28, 42], the absorption coefficient ( $\alpha$ , see ESM, section S-2.2) undergoes a systematic increase with the adopted processing temperature, *i.e.* according to the order **300<400<300\_A<400\_A** (see Table 1). This enhancement is of great importance, taking into account that a superior Vis light absorption efficiency is one of the key factors positively influencing PEC performances [5, 28, 29, 42]. In particular, this phenomenon has been traced back to an increase of light scattering for the formation of hierarchical structures, as previously discussed [20]. The increase of light absorption, however, cannot be traced back to

the sole increase in particle size observed by FE-SEM analyses [28] and is also determined by an increase in the system crystallinity with processing temperature (compare XRD and TEM results, Figures 1 and 7).

The effects of the processing temperature on light absorption properties was further evidenced by the Tauc plots reported in the inset of Figure 6 (see also ESM), enabling to extrapolate optical band-gaps. The  $E_G$  values, in good agreement with previous reports on *hematite* [4, 9, 18, 19, 30, 35, 36], decrease according to the order **300>400>300\_A>400\_A** (see Table 1). In addition, a slight increase in the slope of the transition upon annealing (see Figure 5) was also observed. In the Tauc relation (equation S-1 in the ESM), the slope is proportional to the band tailing parameter, which, in turn, is related to the distribution of energy states near the valence and conduction band edges [28]. Its increase, as well as the above band-gap variations, are both due to an increased material crystallinity and particle size occurring after thermal treatment [10, 53, 54].

Further important clues are provided by an analysis of the optical penetration depth ( $\alpha^{-1}$ ) values (defined as the distance over which 63% of the photons of wavelength  $\lambda$  are absorbed [33, 46]; Table 1, and ESM). The values obtained at  $\lambda = 500$  nm (Table 1) agree reasonably well with previous data for  $\alpha$ -Fe<sub>2</sub>O<sub>3</sub> systems [10, 44]. In the present study,  $\alpha^{-1}$  values monotonically decrease according to the order **300>400>300\_A>400\_A**, likely resulting in an enhanced system photoefficiency [7, 44].

PEC performances of the target materials were evaluated by measuring the current-voltage characteristics in the dark and under irradiation. In general, dark currents (not reported) are two orders of magnitude lower than the ones under illumination. Photocurrent density vs. applied voltage curves for front side illumination are displayed in Figure 6. Irrespective of the deposition temperature, a systematic photoresponse increase is observed upon thermal treatment, indicating a beneficial influence of the latter on functional performances. For

300°C-grown materials (Figure 6a), photocurrent values undergo an appreciable enhancement after annealing (compare Table 1). For samples fabricated at 400°C, the resulting photocurrent increase upon thermal treatment was lower (nearly 5-fold), but higher  $j$  values were obtained after annealing (compare  $j$  values of **300\_A** vs. **300** and of **400\_A** vs. **400** in Table 1). In this case, the photocurrent onset shifts by about 0.1 V to negative potential after annealing, improving thus the  $j$  values at lower bias voltages, as recently reported for *hematite*-based nanosheet arrays [42].

Despite some investigators obtained higher photocurrent values for Fe<sub>2</sub>O<sub>3</sub>-based materials [4, 11, 13, 19, 20], the photoefficiency of the **400\_A** specimen ( $j \approx 680 \mu\text{A cm}^{-2}$  at 1.50 V) compares favorably not only with various bare Fe<sub>2</sub>O<sub>3</sub> photoelectrodes treated at similar temperatures [1, 5, 9, 10, 16, 22, 28, 36, 42, 44], but also with some *hematite* films either doped [15, 17, 18, 30, 33] or functionalized [12, 23, 34]. This finding highlights the potential of the proposed fabrication route for the production of  $\alpha$ -Fe<sub>2</sub>O<sub>3</sub> photoanodes with reasonable efficiency even without any dopants, under milder annealing conditions ( $T < 700^\circ\text{C}$ ) than those often reported.

Subsequently, in a preliminary attempt to further optimize the present *hematite* systems [11], the most active sample, *i.e.* **400\_A**, was additionally functionalized with Co-Pi [ESM, Section S-1], a well-known oxygen evolution catalyst [21, 34, 35]. As shown in Figure 6b, upon functionalization with Co-Pi the photocurrent density at 1.23 V vs. RHE undergoes an 80% enhancement, and the potential shows a cathodic shift of  $\approx 0.2$  V. In line with previous reports on *hematite* functionalized by Co-Pi [16, 29, 35], Ir oxide [11] or NiFeO<sub>x</sub> [26], these variations reflect the activity of Co-Pi as a catalyst for the oxygen evolution reaction, speeding up the reaction kinetics and reducing carrier recombination [16, 34].

Overall, PEC data discussed so far indicate that the system photoresponse increases according to the following order: **300** < **400** < **300\_A** < **400\_A** (see Table 1). The

photoefficiency improvement with increasing processing temperature can be ascribed to a concurrence of different effects [5, 13, 20, 28, 30, 35]:

- i) the increase in crystallinity and in the (110) preferential orientation, following the same order **300**<**400**<**300\_A**<**400\_A** (compare XRD/TEM results and Table 1);
- ii) the morphological rearrangement evidenced by FE-SEM data (see Figure 4 and the related discussion), with particular regard to the porosity increase and the concomitant reduction of grain boundary density;
- iii) the systematic enhancement of the absorption coefficient with annealing temperature and the parallel decrease of the optical band-gap (see Figure 5 and Table 1).

The information gathered so far can explain the obtained order of PEC performances for the samples. Nevertheless, other factors, such as electron transport limitations and recombination centres, can play a crucial role in determining the functional behavior of *hematite* [7]. In this regard, a further investigation of the system nano-scale evolution upon annealing and of its impact on the photo-generated charge carrier kinetics is of major importance. In order to gain a deeper insight into these issues, TEM and TAS analyses were carried out on two selected samples, namely **300** and **300\_A**. These specimens were chosen taking into account that they present a higher photoresponse increase upon annealing with respect to nanodeposits fabricated at 400°C (see Figure 6 and Table 1).

The nanoscale morphology and composition of the selected  $\alpha$ -Fe<sub>2</sub>O<sub>3</sub> deposits was investigated by TEM. Figures 7a-b display HAADF-STEM images, also referred to as Z-contrast or mass-thickness contrast images, of as-prepared and annealed materials. The samples clearly consist of three layers, a glass substrate, the FTO layer and the top Fe<sub>2</sub>O<sub>3</sub> nanodeposit, whose chemical nature is confirmed by the pertaining EDX map (Figure 7a, inset, and Figure S-4 in the ESM). In agreement with XRD data (see above), ED characterization (Figure 7c, inset) confirms that the only crystalline phase is  $\alpha$ -Fe<sub>2</sub>O<sub>3</sub> [50]. The electron diffraction rings of the

as-prepared sample demonstrate the polycrystalline nature of the  $\text{Fe}_2\text{O}_3$  system.

A detailed inspection demonstrates that thermal treatment induces a significant increase of the nanodeposits porosity, a very beneficial effect in terms of PEC performances (compare Figure 6 and the above discussion). Before thermal treatment (Figures 7a and c), the  $\alpha\text{-Fe}_2\text{O}_3$  nanodeposit was thinner and relatively dense (see also Table 1). In a different way, the homologous annealed system (Figures 7b and d) appears less dense and forms dendritic structures (see also FE-SEM data). The presence of low-contrast pores inside the target nanostructures can also be clearly observed (see Figure 7d). Additionally, the crystallinity undergoes a parallel enhancement upon annealing, as illustrated by the high resolution HAADF-STEM image of a typical  $\alpha\text{-Fe}_2\text{O}_3$  dendrite (Figure 7e), in agreement with the XRD data. The inset Fourier Transform pattern confirms that the dendrite is imaged along the  $[100]$   $\alpha\text{-Fe}_2\text{O}_3$  zone axis orientation. The preferred exposure of  $\{110\}$ -type surface facets, as suggested by XRD results, is a result of the near  $c$ -oriented growth of most of the dendrites (see also Figure S-5 in the ESM).

In order to gain insight into the kinetics of photo-produced charge carriers, TAS analyses were carried out on specimens deposited at  $300^\circ\text{C}$ , before and after annealing. Figure 8 shows the transient absorption decays of the *hematite* photoelectrodes, following the band-gap excitation laser pulse. On a ms timescale (Figure 8a) a strong absorption bleaching (negative absorption change) was observed, attributed to a decreased ground state absorption caused, in turn, by trapped photoelectrons a few hundred mV below the conduction band edge [25, 40, 41]. Exponential fits of the bleaching recovery (Figure 8c) yielded lifetimes of  $1.7 \pm 0.4\text{ms}$  and  $1.9 \pm 0.7\text{ ms}$  for as-prepared and annealed specimens, respectively, suggesting similar recombination dynamics on a ms timescale. The main difference between these TAS signals is the strong transient absorption observed for the annealed sample 5 ms after excitation, which is even more pronounced on a second timescale (Figure 8b). The

positive absorption change corresponds to photo holes surviving bulk recombination, possessing a sufficient lifetime to participate to the PEC H<sub>2</sub>O splitting (Figure 8d) [14]. Using a simple mono-exponential fit, a lifetime of  $3 \pm 1$  s is determined for photogenerated holes contributing to water oxidation. As observed in Figure 8b, the number of long-lived holes appreciably increases after annealing, providing a key explanation on the impact of annealing on the charge carrier lifetime.

Figure 8c presents absorption decay component spectra of *hematite* photoelectrodes derived by global mono- (**300**) and bi-exponential fits (**300\_A**) of transient decays on a ms timescale and the calculated transient spectrum at 0 ms delay. The bi-exponential model was adopted to fit also the decay of positive transient hole absorption of the annealed sample (Figure 8b). The transient spectra at 0 ms and  $\tau_1 = 1.7$  ms of trapped electrons at  $\lambda = 580$  nm and photoholes at  $\lambda > 650$  nm are similar for both samples suggesting an equal number of charges in the sub-ms timescale, indicating that thermal treatments do not alter primary electron-hole recombination processes on a time range faster than  $\mu$ s.

The transient component spectrum of  $\tau_1 = 1.9$  ms is mainly attributed to recombination of the photoelectrons resulting in the final transient state of  $\tau_2 = 3$  s (**300\_A**) in Figure 8c. The broad and shapeless transient absorption of the final state corresponds to the absorption of long-lived holes with no remaining trapped electron absorption at  $\lambda = 580$  nm. The absorption amplitude indicates that roughly half of the holes in a ms timescale (spectrum at 0 ms) survive to the recombination processes, and have a lifetime in the second time range. The bleaching recovery, *i.e.* the disappearance of photo-generated trapped electron absorption, is due to electron extraction into the external electrical circuit [25, 41], resulting in photoholes with a prolonged lifetime of 3 s. The obtained lifetime is in line with previously reported values for similar systems [2]. Based on these data, thermal treatment is suggested to increase the electron mobility in the target *hematite* systems, thus hindering electron-hole



1 recombination (*i.e.*, producing an enhanced electron extraction). The resulting long-lived  
2 holes contributing to the transient absorption have a sufficient lifetime to participate to the  
3  
4 PEC H<sub>2</sub>O oxidation (Figure 8d), as reflected by the significant photo response enhancement  
5  
6 after annealing (Figure 6). Conversely, the as-prepared **300** photoelectrode has a negligible  
7  
8 PEC activity, as there was no evidence of long-lived photo holes.  
9  
10

### 11 **3. Conclusions**

12  
13 Single phase *hematite* nanostructures were fabricated on FTO substrates *via* single-step PE-  
14  
15 CVD at temperatures of 300 and 400°C, followed by thermal treatment in air at 650°C. The  
16  
17 proposed approach yields system with hierarchical morphologies, that can be finely tailored  
18  
19 as a function of the annealing process, resulting in an increase of the system porosity.  
20  
21 Furthermore, the systems present a (110) orientation progressively enhanced by the  
22  
23 processing temperature. Accordingly, the best performing systems in PEC H<sub>2</sub>O splitting were  
24  
25 the most crystalline materials, characterized by the highest porosity and light harvesting  
26  
27 capabilities, along with the lowest band-gap and optical penetration depth values. The  
28  
29 annealing process also has a drastic effect on the dynamics of photogenerated charge carriers,  
30  
31 resulting in long-lived holes with lifetimes > 1 s, positively contributing to water oxidation.  
32  
33 The system functional performances can be further improved by functionalization with a Co-  
34  
35 Pi overlayer, which has a beneficial effect in amplifying the measured photocurrent and  
36  
37 reducing the onset potential.  
38  
39

40  
41 Our results demonstrate the possibility of tailoring the PEC water splitting activity of  $\alpha$ -  
42  
43 Fe<sub>2</sub>O<sub>3</sub> photoelectrodes, providing useful clues on the important parameters to be tuned in  
44  
45 order to develop more efficient PEC devices. In particular, the activities of the present  
46  
47 systems are prone to further increase by optimization of the synthetic procedure, with  
48  
49  
50  
51  
52  
53  
54  
55  
56  
57  
58  
59  
60  
61  
62  
63  
64  
65

1 particular focus on lower feature sizes, closer to the hole diffusion length. Further efforts will  
2 be also devoted to the introduction of metal dopants and the functionalization with suitable  
3 layers, as well as to  $\text{Fe}_2\text{O}_3$  growth onto three-dimensional structures. This will lead to a  
4 higher performance boost in the sustainable storage of solar energy through water splitting.  
5  
6  
7  
8  
9

## 10 11 12 **Acknowledgements**

13  
14  
15  
16 The authors acknowledge financial support under the Seventh Framework Program (FP7) by  
17 the project “SOLAROGENIX” (NMP4-SL-2012-310333) and the ERC grant N°246791 –  
18 COUNTATOMS. This work was further funded by Padova University ex-60% 2012-2014  
19 and SOLLEONE (CPDR132937/13) projects, as well as by Regione Lombardia-INSTM  
20 ATLANTE program and the fund for scientific research Flanders (FWO). Many thanks are  
21 also due to Prof. J.R. Morante, Dr. D. Monllor-Satoca, Dr. C. Fàbrega and Dr. T. Andreu  
22 (IREC, Sant Adrià de Besòs, Spain) for the precious help and assistance in PEC  
23 measurements.  
24  
25  
26  
27  
28  
29  
30  
31  
32  
33  
34  
35  
36  
37  
38

39 **Electronic Supplementary Material:** Supplementary material (with additional synthetic  
40 details, characterisation and discussion) is available in the online version of this article at  
41 [http://dx.doi.org/10.1007/\\*\\*\\*\\*\\*](http://dx.doi.org/10.1007/*****)  
42  
43  
44  
45  
46  
47  
48  
49  
50  
51  
52  
53  
54  
55  
56  
57  
58  
59  
60  
61  
62  
63  
64  
65

## References

- [1] Riha, S. C.; Klahr, B. M.; Tyo, E. C.; Seifert, S.; Vajda, S.; Pellin, M. J.; Hamann, T. W.; Martinson, A. B. F. Atomic layer deposition of a submonolayer catalyst for the enhanced photoelectrochemical performance of water oxidation with hematite. *ACS Nano* **2013**, *7*, 2396-2405.
- [2] Cowan, A. J.; Barnett, C. J.; Pendlebury, S. R.; Barroso, M.; Sivula, K.; Grätzel, M.; Durrant, J. R.; Klug, D. R. Activation energies for the rate-limiting step in water photooxidation by nanostructured  $\alpha$ -Fe<sub>2</sub>O<sub>3</sub> and TiO<sub>2</sub>. *J. Am. Chem. Soc.* **2011**, *133*, 10134-10140.
- [3] Lee, J.; Mubeen, S.; Ji, X.; Stucky, G. D.; Moskovits, M. Plasmonic photoanodes for solar water splitting with visible light. *Nano Lett.* **2012**, *12*, 5014-5019.
- [4] Mirbagheri, N.; Wang, D.; Peng, C.; Wang, J.; Huang, Q.; Fan, C.; Ferapontova, E. E. Visible light driven photoelectrochemical water oxidation by Zn- and Ti-doped hematite nanostructures. *ACS Catal.* **2014**, *4*, 2006-2015.
- [5] Ling, Y.; Wang, G.; Wheeler, D. A.; Zhang, J. Z.; Li, Y. Sn-doped hematite nanostructures for photoelectrochemical water splitting. *Nano Lett.* **2011**, *11*, 2119-2125.
- [6] Wheeler, D. A.; Wang, G.; Ling, Y.; Li, Y.; Zhang, J. Z. Nanostructured hematite: synthesis, characterization, charge carrier dynamics, and photoelectrochemical properties. *Energy Environ. Sci.* **2012**, *5*, 6682-6702.
- [7] Hahn, N. T.; Ye, H.; Flaherty, D. W.; Bard, A. J.; Mullins, C. B. Reactive ballistic deposition of  $\alpha$ -Fe<sub>2</sub>O<sub>3</sub> thin films for photoelectrochemical water oxidation. *ACS Nano* **2010**, *4*, 1977-1986.
- [8] Mettenbörger, A.; Singh, T.; Singh, A. P.; Järvi, T. T.; Moseler, M.; Valldor, M.; Mathur, S. Plasma-chemical reduction of iron oxide photoanodes for efficient solar hydrogen production. *Int. J. Hydrogen Energy* **2014**, *39*, 4828-4835.
- [9] Singh, A. P.; Mettenbörger, A.; Golus, P.; Mathur, S. Photoelectrochemical properties of hematite films grown by plasma enhanced chemical vapor deposition. *Int. J. Hydrogen Energy* **2012**, *37*, 13983-13988.
- [10] Rajendran, R.; Yaakob, Z.; Pudukudy, M.; Rahaman, M. S. A.; Sopian, K. Photoelectrochemical water splitting performance of vertically aligned hematite nanoflakes deposited on FTO by a hydrothermal method. *J. All. Compd.* **2014**, *608*, 207-212.

- [11] Marelli, M.; Naldoni, A.; Minguzzi, A.; Allieta, M.; Virgili, T.; Scavia, G.; Recchia, S.; Psaro, R.; Dal Santo, V. Hierarchical hematite nanoplatelets for photoelectrochemical water splitting. *ACS Appl. Mater. Interfaces* **2014**, *6*, 11997-12004.
- [12] Steier, L.; Herraiz-Cardona, I.; Gimenez, S.; Fabregat-Santiago, F.; Bisquert, J.; Tilley, S. D.; Grätzel, M. Understanding the role of underlayers and overlayers in thin film hematite photoanodes. *Adv. Funct. Mater.* **2014**, DOI: 10.1002/adfm.201402742.
- [13] Kim, J. Y.; Magesh, G.; Youn, D. H.; Jang, J.-W.; Kubota, J.; Domen, K.; Lee, J. S. Single-crystalline, wormlike hematite photoanodes for efficient solar water splitting. *Sci. Rep.* **2013**, *3*, 2681.
- [14] Cowan, A. J.; Durrant, J. R. Long-lived charge separated states in nanostructured semiconductor photoelectrodes for the production of solar fuels. *Chem. Soc. Rev.* **2013**, *42*, 2281-2293.
- [15] Dunn, H. K.; Feckl, J. M.; Muller, A.; Fattakhova-Rohlfing, D.; Morehead, S. G.; Roos, J.; Peter, L. M. P.; Scheu, C.; Bein, T. Tin doping speeds up hole transfer during light-driven water oxidation at hematite photoanodes. *Phys. Chem. Chem. Phys.* **2014**, *16*, 24610-24620.
- [16] Hamann, T. W. Splitting water with rust: hematite photoelectrochemistry. *Dalton Trans.* **2012**, *41*, 7830-7834.
- [17] Liu, J.; Liang, C.; Xu, G.; Tian, Z.; Shao, G.; Zhang, L. Ge-doped hematite nanosheets with tunable doping level, structure and improved photoelectrochemical performance. *Nano Energy* **2013**, *2*, 328-336.
- [18] Shen, S.; Kronawitter, C.; Jiang, J.; Mao, S.; Guo, L. Surface tuning for promoted charge transfer in hematite nanorod arrays as water-splitting photoanodes. *Nano Res.* **2012**, *5*, 327-336.
- [19] Hsu, Y.-P.; Lee, S.-W.; Chang, J.-K.; Tseng, C.-J.; Lee, K.-R.; Wang, C.-H. Effects of platinum doping on the photoelectrochemical properties of Fe<sub>2</sub>O<sub>3</sub> Electrodes. *Int. J. Electrochem. Sci.* **2013**, *8*, 11615-11623.
- [20] Park, S.; Kim, H. J.; Lee, C. W.; Song, H. J.; Shin, S. S.; Seo, S. W.; Park, H. K.; Lee, S.; Kim, D.-W.; Hong, K. S. Sn self-doped  $\alpha$ -Fe<sub>2</sub>O<sub>3</sub> nanobranched arrays supported on a transparent, conductive SnO<sub>2</sub> trunk to improve photoelectrochemical water oxidation. *Int. J. Hydrogen Energy* **2014**, *39*, 16459-16467.
- [21] Sivula, K.; Le Formal, F.; Grätzel, M. Solar water splitting: progress using hematite ( $\alpha$ -Fe<sub>2</sub>O<sub>3</sub>) Photoelectrodes. *ChemSusChem* **2011**, *4*, 432-449.

- [22] Liu, J.; Shahid, M.; Ko, Y.-S.; Kim, E.; Ahn, T. K.; Park, J. H.; Kwon, Y.-U. Investigation of porosity and heterojunction effects of a mesoporous hematite electrode on photoelectrochemical water splitting. *Phys. Chem. Chem. Phys.* **2013**, *15*, 9775-9782.
- [23] Tallarida, M.; Das, C.; Cibrev, D.; Kukli, K.; Tamm, A.; Ritala, M.; Lana-Villarreal, T.; Gómez, R.; Leskelä, M.; Schmeisser, D. Modification of hematite electronic properties with trimethyl aluminum to enhance the efficiency of photoelectrodes. *J. Phys. Chem. Lett.* **2014**, 3582-3587.
- [24] LaTempa, T. J.; Feng, X.; Paulose, M.; Grimes, C. A. Temperature-dependent growth of self-assembled hematite ( $\alpha$ -Fe<sub>2</sub>O<sub>3</sub>) nanotube arrays: rapid electrochemical synthesis and photoelectrochemical properties. *J. Phys. Chem. C* **2009**, *113*, 16293-16298.
- [25] Le Formal, F.; Pendlebury, S. R.; Cornuz, M.; Tilley, S. D.; Grätzel, M.; Durrant, J. R. Back electron-hole recombination in hematite photoanodes for water splitting. *J. Am. Chem. Soc.* **2014**, *136*, 2564-2574.
- [26] Du, C.; Yang, X.; Mayer, M. T.; Hoyt, H.; Xie, J.; McMahon, G.; Bischoff, G.; Wang, D. Hematite-based water splitting with low turn-on voltages. *Ang. Chem. Int. Ed.* **2013**, *52*, 12692-12695.
- [27] Nasibulin, A.; Rackauskas, S.; Jiang, H.; Tian, Y.; Mudimela, P.; Shandakov, S.; Nasibulina, L.; Jani, S.; Kauppinen, E. Simple and rapid synthesis of  $\alpha$ -Fe<sub>2</sub>O<sub>3</sub> nanowires under ambient conditions. *Nano Res.* **2009**, *2*, 373-379.
- [28] Sivula, K.; Zboril, R.; Le Formal, F.; Robert, R.; Weidenkaff, A.; Tucek, J.; Frydrych, J.; Grätzel, M. Photoelectrochemical water splitting with mesoporous hematite prepared by a solution-based colloidal approach. *J. Am. Chem. Soc.* **2010**, *132*, 7436-7444.
- [29] Qiu, Y.; Leung, S.-F.; Zhang, Q.; Hua, B.; Lin, Q.; Wei, Z.; Tsui, K.-H.; Zhang, Y.; Yang, S.; Fan, Z. Efficient photoelectrochemical water splitting with ultrathin films of hematite on three-dimensional nanophotonic structures. *Nano Lett.* **2014**, *14*, 2123-2129.
- [30] Shen, S.; Jiang, J.; Guo, P.; Kronawitter, C. X.; Mao, S. S.; Guo, L. Effect of Cr doping on the photoelectrochemical performance of hematite nanorod photoanodes. *Nano Energy* **2012**, *1*, 732-741.
- [31] Gao, G.; Zhang, Q.; Wang, K.; Song, H.; Qiu, P.; Cui, D. Axial compressive  $\alpha$ -Fe<sub>2</sub>O<sub>3</sub> microdisks prepared from CSS template for potential anode materials of lithium ion batteries. *Nano Energy* **2013**, *2*, 1010-1018.

- [32] Low, Q. X.; Ho, G. W. Facile structural tuning and compositing of iron oxide-graphene anode towards enhanced supacapacitive performance. *Nano Energy* **2014**, *5*, 28-35.
- [33] Cesar, I.; Sivula, K.; Kay, A.; Zboril, R.; Grätzel, M. Influence of feature size, film thickness, and silicon doping on the performance of nanostructured hematite photoanodes for solar water splitting. *J. Phys. Chem. C* **2009**, *113*, 772-782.
- [34] Fu, L.; Yu, H.; Zhang, C.; Shao, Z.; Yi, B. Cobalt phosphate group modified hematite nanorod array as photoanode for efficient solar water splitting. *Electrochim. Acta* **2014**, *136*, 363-369.
- [35] Wang, L.; Lee, C.-Y.; Schmuki, P. Influence of annealing temperature on photoelectrochemical water splitting of  $\alpha$ -Fe<sub>2</sub>O<sub>3</sub> films prepared by anodic deposition. *Electrochim. Acta* **2013**, *91*, 307-313.
- [36] Fu, Z.; Jiang, T.; Liu, Z.; Wang, D.; Wang, L.; Xie, T. Highly photoactive Ti-doped  $\alpha$ -Fe<sub>2</sub>O<sub>3</sub> nanorod arrays photoanode prepared by a hydrothermal method for photoelectrochemical water splitting. *Electrochim. Acta* **2014**, *129*, 358-363.
- [37] Pendlebury, S. R.; Cowan, A. J.; Barroso, M.; Sivula, K.; Ye, J.; Gratzel, M.; Klug, D. R.; Tang, J.; Durrant, J. R. Correlating long-lived photogenerated hole populations with photocurrent densities in hematite water oxidation photoanodes. *Energy Environ. Sci.* **2012**, *5*, 6304-6312.
- [38] Joly, A. G.; Williams, J. R.; Chambers, S. A.; Xiong, G.; Hess, W. P.; Laman, D. M. Carrier dynamics in  $\alpha$ -Fe<sub>2</sub>O<sub>3</sub> (0001) thin films and single crystals probed by femtosecond transient absorption and reflectivity. *J. Appl. Phys.* **2006**, *99*.
- [39] He, Y. P.; Miao, Y. M.; Li, C. R.; Wang, S. Q.; Cao, L.; Xie, S. S.; Yang, G. Z.; Zou, B. S.; Burda, C. Size and structure effect on optical transitions of iron oxide nanocrystals. *Phys. Rev. B* **2005**, *71*, 125411.
- [40] Pendlebury, S. R.; Wang, X.; Le Formal, F.; Cornuz, M.; Kafizas, A.; Tilley, S. D.; Grätzel, M.; Durrant, J. R. Ultrafast charge carrier recombination and trapping in hematite photoanodes under applied bias. *J. Am. Chem. Soc.* **2014**, *136*, 9854-9857.
- [41] Barroso, M.; Pendlebury, S. R.; Cowan, A. J.; Durrant, J. R. Charge carrier trapping, recombination and transfer in hematite ( $\alpha$ -Fe<sub>2</sub>O<sub>3</sub>) water splitting photoanodes. *Chem. Sci.* **2013**, *4*, 2724-2734.

- [42] Liu, J.; Cai, Y. Y.; Tian, Z. F.; Ruan, G. S.; Ye, Y. X.; Liang, C. H.; Shao, G. S. Highly oriented Ge-doped hematite nanosheet arrays for photoelectrochemical water oxidation. *Nano Energy* **2014**, 9, 282-290.
- [43] Cornuz, M.; Grätzel, M.; Sivula, K. Preferential orientation in hematite films for solar hydrogen production via water splitting. *Chem. Vap. Deposition* **2010**, 16, 291-295.
- [44] Barreca, D.; Carraro, G.; Gasparotto, A.; Maccato, C.; Sada, C.; Singh, A. P.; Mathur, S.; Mettenbörger, A.; Bontempi, E.; Depero, L. E. Columnar Fe<sub>2</sub>O<sub>3</sub> arrays via plasma-enhanced growth: interplay of fluorine substitution and photoelectrochemical properties. *Int. J. Hydrogen Energy* **2013**, 38, 14189-14199.
- [45] Park, S.; Kim, D.; Lee, C.; Seo, S.-D.; Kim, H.; Han, H.; Hong, K.; Kim, D.-W. Surface-area-tuned, quantum-dot-sensitized heterostructured nanoarchitectures for highly efficient photoelectrodes. *Nano Res.* **2014**, 7, 144-153.
- [46] Carraro, G.; Gasparotto, A.; Maccato, C.; Bontempi, E.; Bilo, F.; Peeters, D.; Sada, C.; Barreca, D. A plasma-assisted approach for the controlled dispersion of CuO aggregates into  $\beta$  iron(III) oxide matrices. *CrystEngComm* **2014**, 16, 8710-8716.
- [47] Tang, J.; Durrant, J. R.; Klug, D. R. Mechanism of photocatalytic water splitting in TiO<sub>2</sub>. Reaction of water with photoholes, importance of charge carrier dynamics, and evidence for four-hole chemistry. *J. Am. Chem. Soc.* **2008**, 130, 13885-13891.
- [48] Tamaki, Y.; Furube, A.; Murai, M.; Hara, K.; Katoh, R.; Tachiya, M. Direct observation of reactive trapped holes in TiO<sub>2</sub> undergoing photocatalytic oxidation of adsorbed alcohols: evaluation of the reaction rates and yields. *J. Am. Chem. Soc.* **2005**, 128, 416-417.
- [49] Moulder, J. F.; Stickle, W. F.; Sobol, P. E.; Bomben, K. D. *Handbook of x-ray photoelectron spectroscopy*; Perkin Elmer Corporation, Eden Prairie, MN, 1992.
- [50] Pattern N° 33-0664 JCPDS (2000).
- [51] Carraro, G.; Maccato, C.; Bontempi, E.; Gasparotto, A.; Lebedev, O. I.; Turner, S.; Depero, L. E.; Van Tendeloo, G.; Barreca, D. Insights on growth and nanoscopic investigation of uncommon iron oxide polymorphs. *Eur. J. Inorg. Chem.* **2013**, 2013, 5454-5461.
- [52] Carraro, G.; Sugrañez, R.; Maccato, C.; Gasparotto, A.; Barreca, D.; Sada, C.; Cruz-Yusta, M.; Sánchez, L. Nanostructured iron(III) oxides: from design to gas- and liquid-phase photo-catalytic applications. *Thin Solid Films* **2014**, 564, 121-127.

- [53] Iribarren, A.; Castro-Rodríguez, R.; Sosa, V.; Peña, J. L. Band-tail parameter modeling in semiconductor materials. *Phys. Rev. B* **1998**, *58*, 1907-1911.
- [54] Iribarren, A.; Castro-Rodríguez, R.; Sosa, V.; Peña, J. L. Modeling of the disorder contribution to the band-tail parameter in semiconductor materials. *Phys. Rev. B* **1999**, *60*, 4758-4762.



Sample ID	Deposition Temperature (°C)	Annealing Temperature (°C)	$I_{(110)}/I_{(012)}$	Mean Nanodeposit Thickness (nm)	Optical band-gap $E_G$ (eV)	Penetration depth @ $\lambda = 500$ nm (nm)	Photocurrent density $j$ ( $\mu\text{A cm}^{-2}$ ) @ 1.23 V <i>vs.</i> RHE)
300	300	-	2.4	$270 \pm 20$	2.10	125	25
400	400	-	3.4	$270 \pm 30$	2.02	85	50
300_A	300	650	4.9	$380 \pm 40$	2.00	70	215
400_A	400	650	5.4	$350 \pm 50$	1.93	65	240

**Table 1** Processing conditions and relevant material properties for the target  $\text{Fe}_2\text{O}_3$  nanodeposits. In all cases, thermal treatments were carried out in air for 1 h (heating rate =  $20^\circ\text{C} \times \text{min}^{-1}$ ). For comparison, the  $I_{(110)}/I_{(012)}$  ratio calculated for the *hematite* powder diffractogram is 2.3 [50].

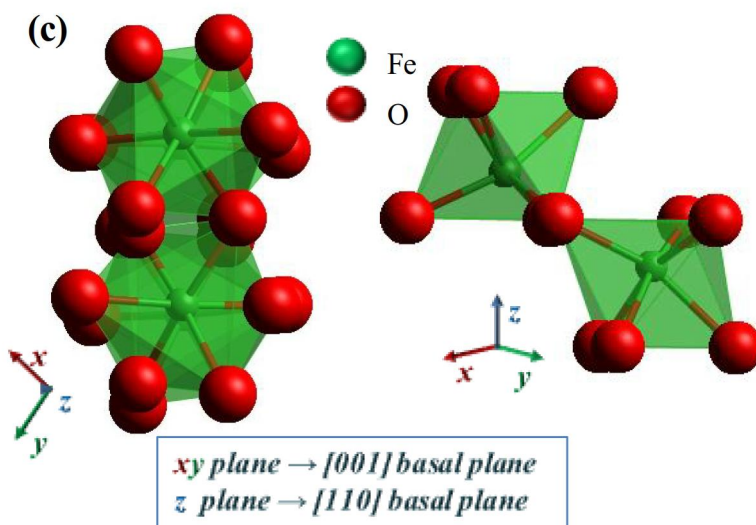
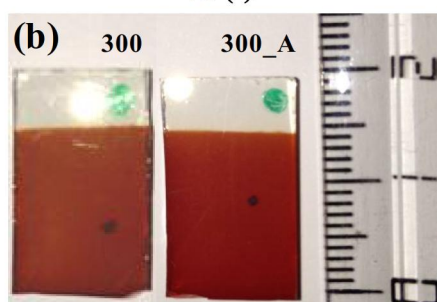
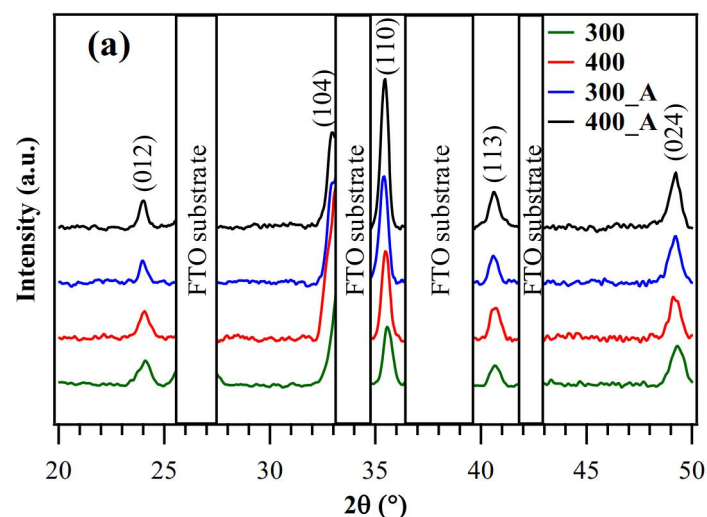


**Figure 1** (a) XRD patterns of as-grown and annealed  $\text{Fe}_2\text{O}_3$  specimens. For sake of clarity, reflections pertaining to the FTO-coated glass substrate are covered. (b) Digital photographs of two obtained photoelectrode specimens before and after thermal treatment. (c) Representation of  $\alpha\text{-Fe}_2\text{O}_3$  structure [50], characterized by octahedral arrangements of iron(III) centres.

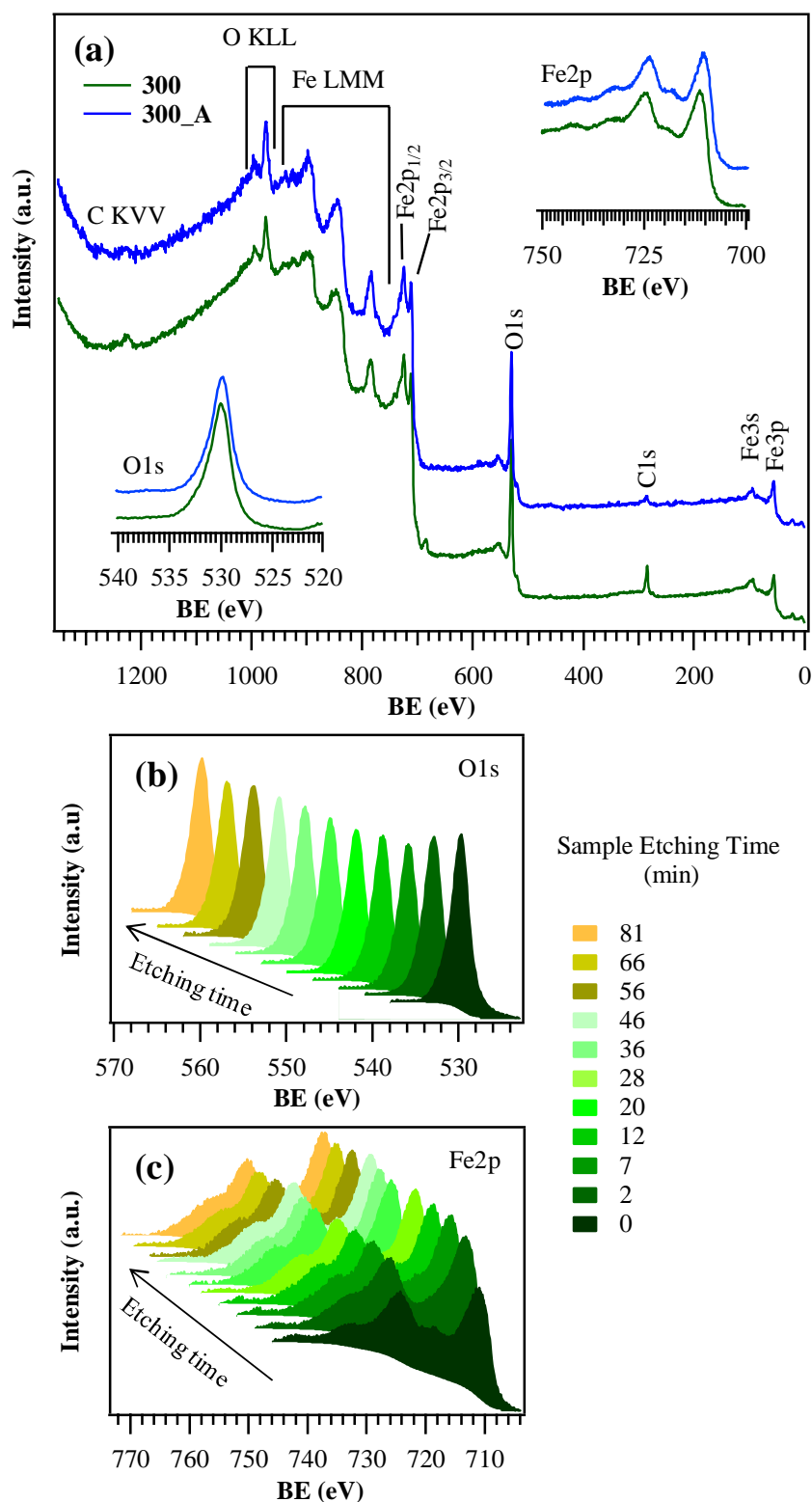


**Figure 2** (a) Representative surface XPS survey spectra for as-prepared and annealed  $\text{Fe}_2\text{O}_3$  specimens grown at  $300^\circ\text{C}$ . Insets display the corresponding Fe2p and O1s spectral regions. XPS depth profiles for the annealed  $\alpha\text{-Fe}_2\text{O}_3$  sample prepared at  $300^\circ\text{C}$ , showing the O1s (b) and Fe2p (c) photopeak evolution as a function of the etching time.

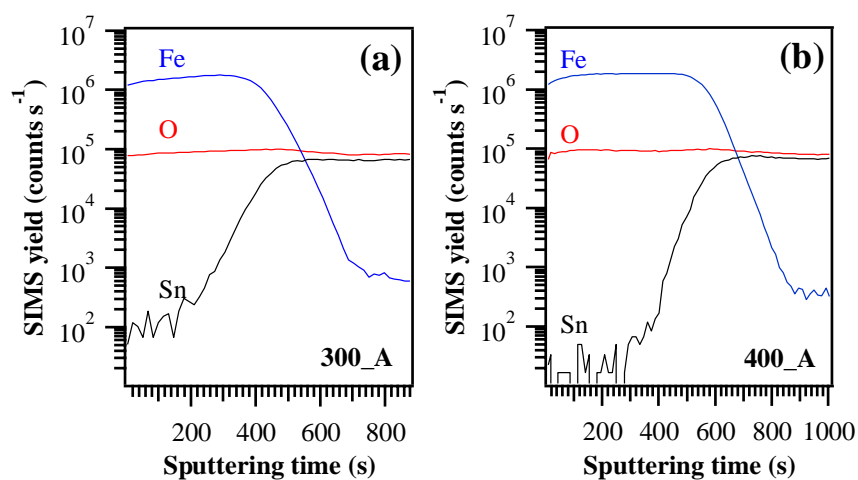


**Figure 3** Fe, O and Sn SIMS depth profiles for  $\text{Fe}_2\text{O}_3$  specimens deposited at  $300^\circ\text{C}$  (a) and  $400^\circ\text{C}$  (b), after thermal treatment.

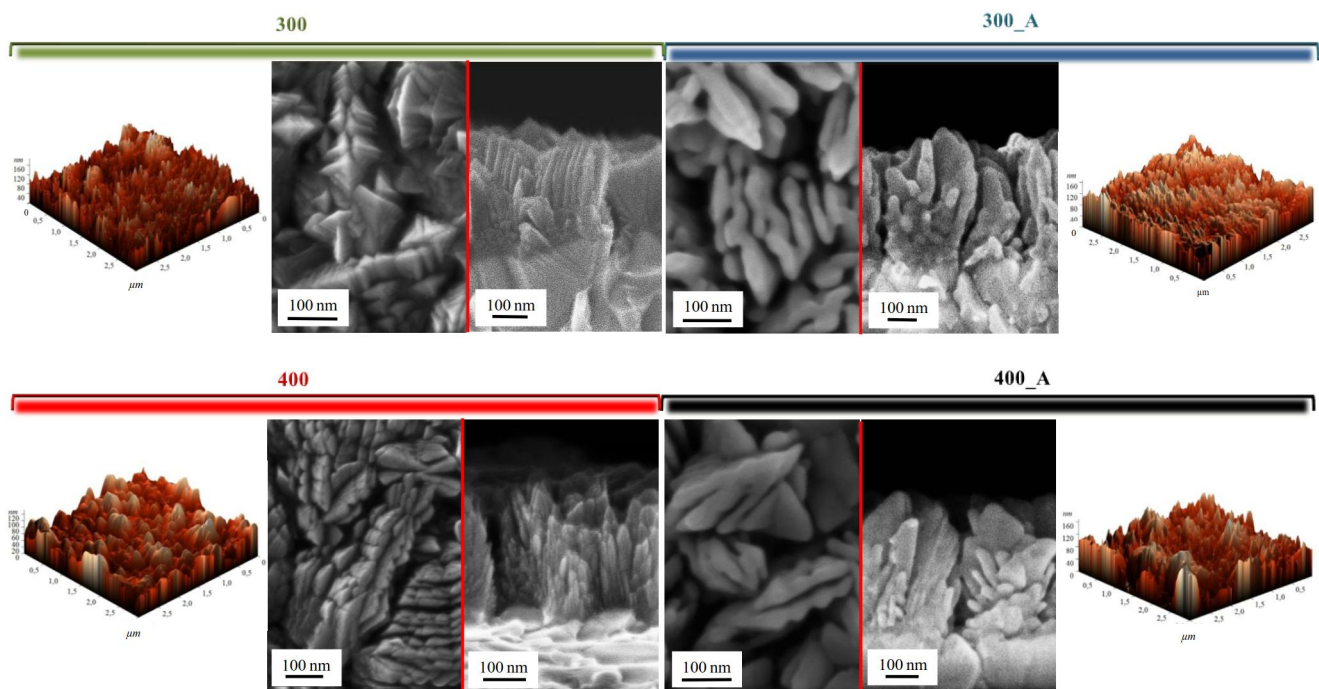


**Figure 4** AFM and FE-SEM images for  $\alpha$ - $\text{Fe}_2\text{O}_3$  nanodeposits grown at 300 and 400°C, before and after thermal treatment.

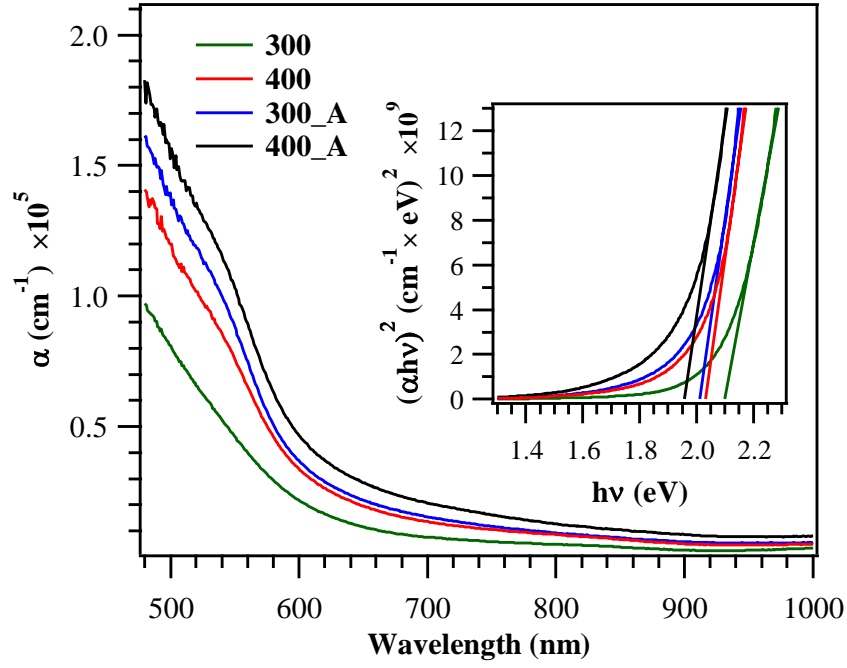


**Figure 5** Optical absorption spectra for as-prepared and annealed  $\text{Fe}_2\text{O}_3$  nanodeposits. Inset: Tauc plot of  $(\alpha h\nu)^2$  vs.  $h\nu$  for the same specimens. The lines fitted to the linear portion of these plots shows the optical band-gap approximation.

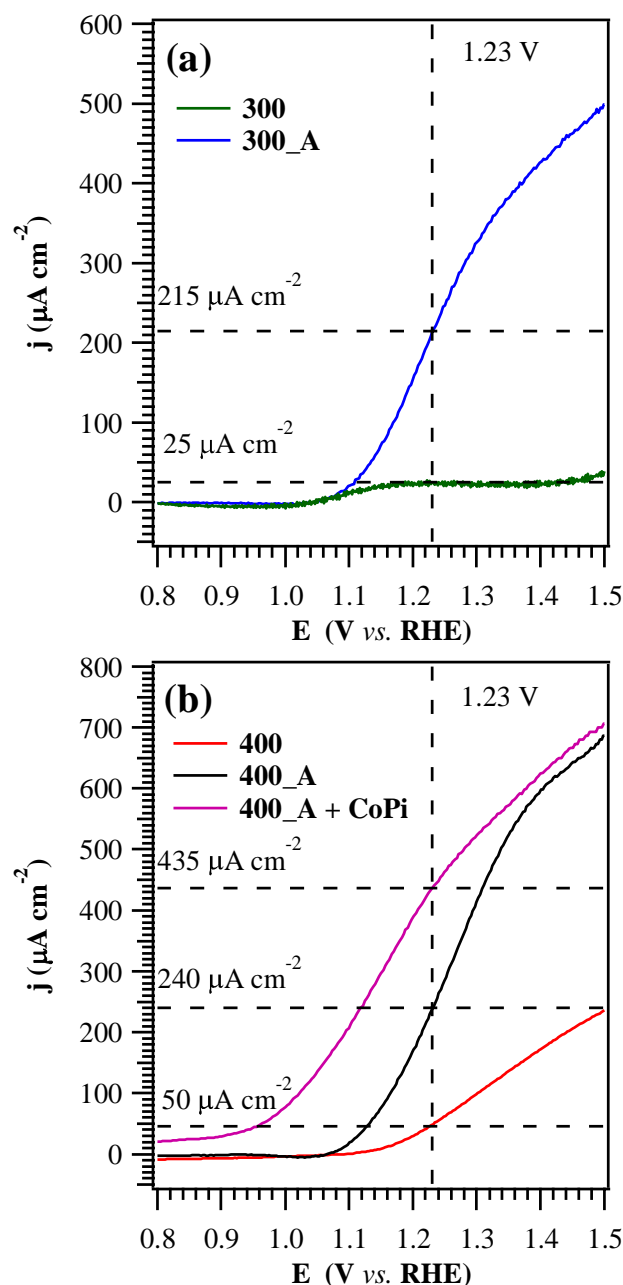


**Figure 6** Photocurrent density vs. applied potential curves for: (a)  $\text{Fe}_2\text{O}_3$  nanodeposits grown at  $300^\circ\text{C}$ , before and after thermal treatment; (b) as-prepared and annealed  $\text{Fe}_2\text{O}_3$  specimens deposited at  $400^\circ\text{C}$ , eventually functionalized with Co-Pi co-catalyst. For sake of clarity, the  $j$  values at 1.23 V vs. RHE (the theoretical water oxidation potential) are marked in each case by dashed lines.

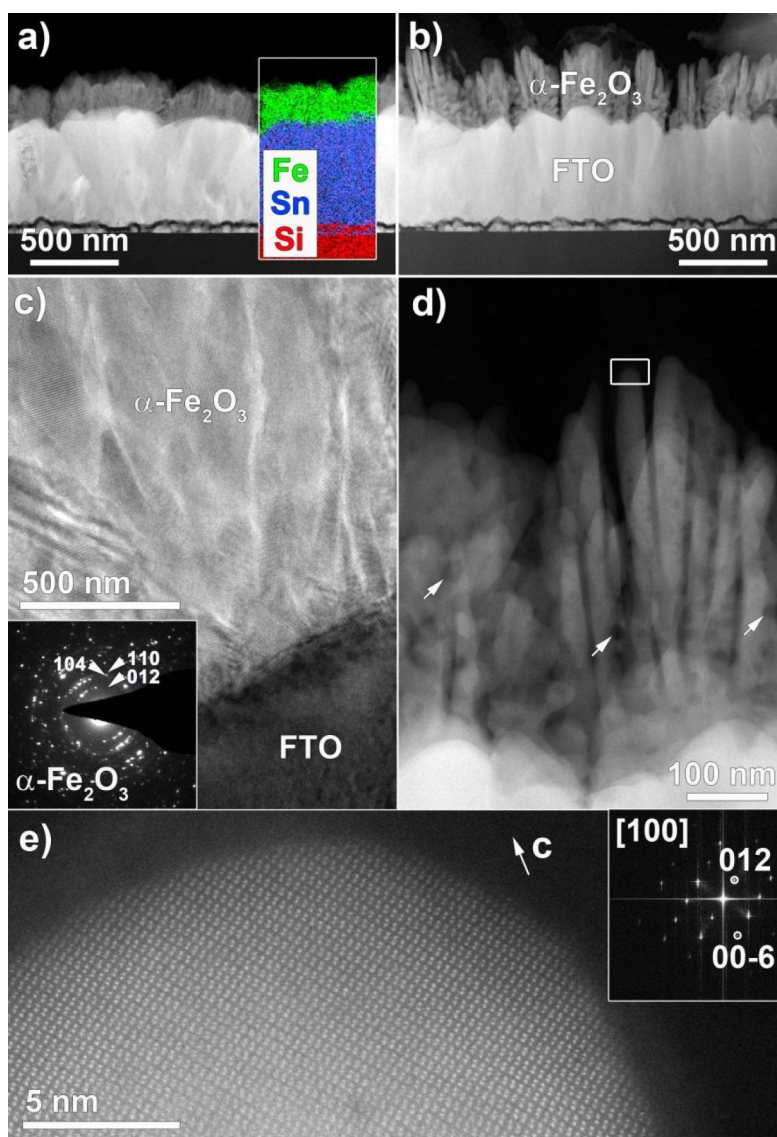


**Figure 7** TEM characterization of as-prepared and annealed  $\alpha$ -Fe<sub>2</sub>O<sub>3</sub> nanodeposits fabricated at 300°C. (a) Cross-sectional HAADF-STEM image of sample **300**, with EDX chemical map displayed in the inset. (b) Cross-sectional HAADF-STEM micrograph of specimen **300\_A**. (c) Bright-field TEM image of the FTO/ $\alpha$ -Fe<sub>2</sub>O<sub>3</sub> interface for sample **300**. Inset: ED pattern of the  $\alpha$ -Fe<sub>2</sub>O<sub>3</sub> nanodeposit. (d) Representative HAADF-STEM image of  $\alpha$ -Fe<sub>2</sub>O<sub>3</sub> dendrites in specimen **300\_A**. White arrows mark the presence of some low-contrast pores. (e) High resolution HAADF-STEM micrograph of a  $\alpha$ -Fe<sub>2</sub>O<sub>3</sub> dendrite in sample **300\_A**. The image is taken from the region marked by the white rectangle in (d).



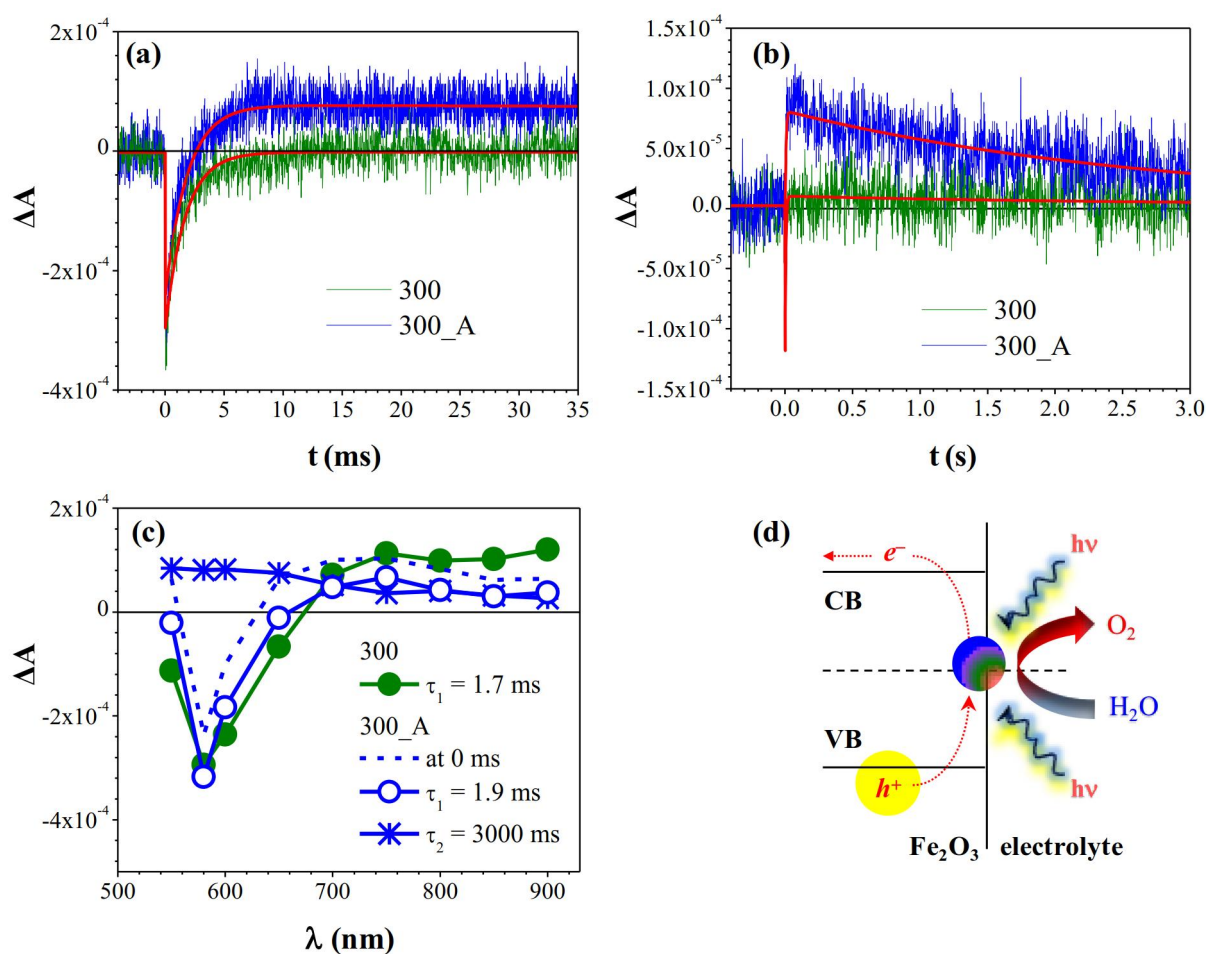


**Figure 8** (a) Transient absorption decays at  $\lambda = 580$  nm on a ms timescale for as-prepared and annealed  $\text{Fe}_2\text{O}_3$  nanodeposits grown at  $300^\circ\text{C}$ . (b) The corresponding decays in a second timescale. Exponential fits are also displayed. (c) Absorption decay component of spectra at 1.6 V vs. RHE for as-prepared and annealed  $\text{Fe}_2\text{O}_3$  nanodeposits grown at  $300^\circ\text{C}$ . The transient absorption spectrum at zero delay time, following the laser pulse excitation, is shown for the **300\_A** sample as the calculated spectrum at 0 ms. (d) Simplified illustration of the photogenerated processes taking place at a photoelectrode-electrolyte interface within the PEC water splitting.